



Detection of the Orbital Modulation of Fe $K\alpha$ Fluorescence Emission in Centaurus X-3 Using the High-resolution Spectrometer Resolve on board XRISM

Yuto Mochizuki^{1,2}, Masahiro Tsujimoto¹, Richard L. Kelley³, Bert Vander Meulen⁴, Teruaki Enoto⁵, Yutaro Nagai⁵, Chris Done⁶, Pragati Pradhan⁷, Natalie Hell⁸, Katja Pottschmidt^{9,10}, Ken Ebisawa^{1,2}, and Ehud Behar¹¹

¹ Institute of Space and Astronautical Science (ISAS), Japan Aerospace Exploration Agency (JAXA), 3-1-1 Yoshinodai, Chuo-ku, Sagami-hara, Kanagawa 252-5210, Japan; mochizuki@ac.jaxa.jp

² Department of Astronomy, Graduate School of Science, The University of Tokyo, 7-3-1 Hongo, Bunkyo-ku, Tokyo 113-0033, Japan

³ X-ray Astrophysics Laboratory, Code 662, NASA Goddard Space Flight Center, 8800 Greenbelt Road, Greenbelt, MD 20771, USA

⁴ Sterrenkundig Observatorium, Universiteit Gent, Krijgslaan 281 S9, 9000 Gent, Belgium

⁵ Department of Physics, Kyoto University, Kitashirakawa-Oiwake-cho, Sakyo-ku, Kyoto, 606-8502, Japan

⁶ Centre for Extragalactic Astronomy, Department of Physics, University of Durham, South Road, Durham DH1 3LE, UK

⁷ Department of Physics, Embry-Riddle Aeronautical University: Prescott, AZ, USA

⁸ Lawrence Livermore National Laboratory, Livermore, CA, USA

⁹ University of Maryland Baltimore County, 1000 Hilltop Circle, Baltimore, MD 21250, USA

¹⁰ CRESST & Astroparticle Physics Laboratory, Code 661, NASA Goddard Space Flight Center, 8800 Greenbelt Road, Greenbelt, MD 20771, USA

¹¹ Physics Department, Technion, Haifa 32000, Israel

Received 2024 September 18; revised 2024 November 12; accepted 2024 November 19; published 2024 December 5

Abstract

The Fe $K\alpha$ fluorescence line emission in X-ray spectra is a powerful diagnostic tool for various astrophysical objects to reveal the distribution of cold matter around photoionizing sources. The advent of the X-ray microcalorimeter on board the XRISM satellite will bring new constraints on the emission line. We present one of the first such results for the high-mass X-ray binary Centaurus X-3, which is composed of an O-type star and a neutron star (NS). We conducted a 155 ks observation covering an entire binary orbit. A weak Fe $K\alpha$ line was detected in all orbital phases at an equivalent width (EW) of 10–20 eV. We found for the first time that its radial velocity (RV) is sinusoidally modulated by the orbital phase. The RV amplitude is $248 \pm 13 \text{ km s}^{-1}$, which is significantly smaller than the value (391 km s^{-1}) expected if the emission is from the NS surface, but is consistent if the emission takes place at the O star surface. We discuss several possibilities of the line production site, including the NS surface, O star surface, O star wind, and accretion stream from the O star to the NS. We ran radiative transfer calculation for some of them assuming spherically symmetric density and velocity profiles and an isotropic distribution of X-ray emission from the NS. None of them explains the observed EW and velocity dispersion dependence on the orbital phase, suggesting that more elaborated modeling is needed. In other words, the present observational results have the capability to constrain deviations from these assumptions.

Unified Astronomy Thesaurus concepts: High energy astrophysics (739); X-ray binary stars (1811); Neutron stars (1108); Radiative transfer (1335)

1. Introduction

In X-ray spectroscopy, the Fe $K\alpha$ line at 6.4 keV is a powerful probe to investigate the distribution of cold matter around X-ray sources. It is fluorescence emission of neutral or low-ionized Fe following the inner-shell ionization by photons above the binding energy of 7.12 keV. Due to the large cosmic abundance and high fluorescence yield of iron, the Fe $K\alpha$ emission line stands out in X-ray spectra of a wide range of objects, including active galactic nuclei, X-ray binaries, cataclysmic variables, and normal stars. In many cases, however, the location of the reprocessing cold matter is a matter of debate. Thus, it is important to characterize the Fe $K\alpha$ emission line complex with observations of higher spectral resolution and signal-to-noise ratio.

The high-energy transmission grating (HETG) spectrometer on board the Chandra X-ray Observatory (C. R. Canizares et al. 2005) was the first to have the capability to resolve the line profile at an energy resolution $R \equiv E/\Delta E \sim 167$ and an

effective area $A_{\text{eff}} \sim 20 \text{ cm}^2$ at 6.4 keV,¹² providing information besides its equivalent width (EW) available with spectrometers with lower energy resolution. Two systematic studies were made on the narrow Fe $K\alpha$ emission from bright X-ray binaries using HETG (J. M. Torrejón et al. 2010; P. Tzanavaris & T. Yaqoob 2018), in which the former argued that the line is unresolved, while the latter argued that it has an FWHM of $\sim 5000 \text{ km s}^{-1}$. These loose constraints are the best that could be achieved even for bright X-ray sources before XRISM.

This has changed drastically with the advent of XRISM X-ray microcalorimeter. With an improved $R \sim 1400$ and $A_{\text{eff}} \sim 174 \text{ cm}^2$ at 6.4 keV, the Resolve instrument (Y. Ishisaki et al. 2022) on board the XRISM satellite (M. S. Tashiro et al. 2020) will reveal new aspects of the emission such as tighter constraints of the line profile, its changes, and the timing delays of line photons compared to continuum photons. These abilities are clearly demonstrated in X-ray binaries hosting a neutron star (NS) by determining how the emission is modulated both by the orbital and spin rotations.

Here, we present the first such result for Centaurus X-3 (Cen X-3), which is an eclipsing high-mass X-ray binary (HMXB)

Original content from this work may be used under the terms of the [Creative Commons Attribution 4.0 licence](https://creativecommons.org/licenses/by/4.0/). Any further distribution of this work must maintain attribution to the author(s) and the title of the work, journal citation and DOI.

¹² <https://cxc.cfa.harvard.edu/proposer/POG/html/index.html>

consisting of an NS and an O6.5 II-III star. The NS was discovered in X-rays (G. Chodil et al. 1967) followed by the O star companion in the optical (W. Krzeminski 1974). The NS is the first X-ray pulsar discovered as such with a spin period $P_{\text{spin}} = 4.8$ s (R. Giacconi et al. 1971). The system parameters are well known. Those we use in this paper are the orbital period $P_{\text{orb}} = 2.08$ days and its change $dP_{\text{orb}}/P_{\text{orb}} = -1.8 \times 10^{-6} \text{ yr}^{-1}$ from the X-ray eclipse timing (E. Schreier et al. 1972; M. Klawin et al. 2023); the mass of the NS and O star $M_{\text{NS}} = 1.21 \pm 0.21 M_{\odot}$ and $M_{\text{O}} = 20.5 \pm 0.7 M_{\odot}$ from the optical radial velocity (RV; T. D. Ash et al. 1999; A. van der Meer et al. 2007); and X-ray pulse timing (R. L. Kelley et al. 1983) measurements modulated by the orbital motion, the semimajor axis length $a = 42.1 \text{ lt-s}$ (L. Bildsten et al. 1997), the inclination angle $i = 70^{\circ}2 \pm 2^{\circ}7$ (T. D. Ash et al. 1999), the ellipticity $e = 0.00$ (R. L. Kelley et al. 1983), and the distance of $D = 6.4$ kpc from a parallax measurement (R. M. Arnason et al. 2021).

2. Observation and Data Reduction

2.1. Instrument

Resolve hosts an array of 6×6 X-ray microcalorimeters based on the HgTe absorber and the Si thermistor thermally anchored to the 50 mK stage at a thermal time constant of ~ 3.5 ms (C. A. Kilbourne et al. 2016), which is maintained with two-stage adiabatic demagnetization refrigerators (ADRs; P. J. Shirron et al. 2016) from the 1.2 K stage by the depressurized superliquid helium stored in the cryostat (Y. Ezoe et al. 2020). One of the pixels (pixel 12) is displaced from the array for calibration purposes. Individual pixels have their own energy gain variation in orbit, which is tracked and corrected (F. S. Porter et al. 2016) using the ^{55}Fe sources placed in one of the filter wheel (FW) windows (C. P. de Vries et al. 2017).

The gate valve (GV) has not yet been opened in orbit, despite several initial attempts. It is an apparatus that keeps the cryostat leak-tight prior to launch and is intended to be opened in orbit. The X-ray transmissive window of the GV is made with Be of a $\sim 250 \mu\text{m}$ thickness (T. Midooka et al. 2021), which restricts the bandpass to above ~ 2 keV. However, this is fortuitous for observations of bright sources like the one presented here since the photon count rates are attenuated in the appropriate dynamic range. Other details of the instrument can be found in K. Sato et al. (2023).

The X-ray microcalorimeter spectrometer excels over CCD-based spectrometers besides R and A_{eff} . Unlike the grating spectrometers on board the Chandra and XMM-Newton observatories, the calibration sources are intermittently illuminated during observations to achieve an energy determination accuracy of $\lesssim 1$ eV. The HgTe absorber provides bandpass to 12 keV and beyond, which is inaccessible with Si absorbers. The event time tagging is accurate to $\sim 5 \mu\text{s}$ (T. Omama et al. 2022) for the need to resolve event pulse shape in time in orbit, which is better than conventional X-ray CCD spectrometers by many orders. The anticoincidence detector discriminates particle-induced events efficiently to reduce the background rate to only one event per spectral resolution (~ 5 eV) per 100 ks (C. A. Kilbourne et al. 2018). All of these contribute to the improved characterization of the Fe $K\alpha$ line and its underlying continuum photons, as will be presented below.

2.2. Observation

The observation (sequence number 300003010) was made from 2024 February 12 23:56:04 to February 15 06:19:04 for a telescope time of 196 ks as a performance verification program. The observation efficiency is very high, 79%, for a satellite in a low Earth orbit as we chose a season when the target is visible without Earth occultation. The XRISM observation covered an entire binary cycle starting from one eclipse to the next (Figure 1(d)). In this Letter, we focus on the Resolve data taken outside the eclipses.

Figure 1(b) shows the light curve in the 2–12 keV band. The eclipses are seen at the beginning and end of the observation. The count rate outside the eclipse shows an average rate of $54\text{--}112 \text{ s}^{-1}$ binned at 100 s. At these rates, the background is negligible (Y. Mochizuki et al. 2024), and the event loss due to the limited computing resources in orbit does not occur (M. Mizumoto et al. 2022).

The X-ray light curve is very stable, which is often seen when the X-ray luminosity is high, $\sim 10^{37} \text{ erg s}^{-1}$, as in the 2006 June observation with XMM-Newton (G. Sanjurjo-Ferrín et al. 2021) and the 2022 July observation with IXPE (M. C. Weisskopf et al. 2022). In other observations, the X-ray light curve is much more variable (S. Suchy et al. 2008; S. Naik et al. 2011; T. Tamba et al. 2023).

2.3. Data Reduction

We retrieved the pipeline products processed with a script version 03.00.011.008. We reduced the data using the HEASOFT package build 7 released for the XRISM science team. For timing analysis, we used all events screened in the standard processing, which amounts to 9.3 million events. For spectroscopy analysis, we applied further event screening to remove events below 0.3 keV, those with too fast or slow pulse rise times for their energy (Y. Mochizuki et al. 2024), those with grades other than high-resolution primary (Hp), and those recorded in pixel 27, which is reported to have an irregular gain trend. A total of 3.6 million events were left. Here, the Hp grade is given for events without any other events within 70.72 ms in the same pixel (Y. Ishisaki et al. 2018). They have the highest accuracy in energy determination and are well calibrated for spectroscopy as of this writing. The Hp branching ratio depends on the concurrent count rate (H. Seta et al. 2012). The average ratio out of the eclipse is ~ 0.39 (Figure 1(c)).

The detector and telescope response files were generated using the `rslmkrmf` and `xaarfgen` tools. No background spectrum was subtracted as it is negligible. Events were divided in time into 16 pieces per orbit that covered $\phi_{\text{orb}} = [\frac{i_{\text{orb}} - 0.5}{16}, \frac{i_{\text{orb}} + 0.5}{16}]$, where $i_{\text{orb}} \in \{-1, 0, 1, \dots, 15\}$ (Figure 1(d)). Among them, $i_{\text{orb}} \in \{3, 4, 5, \dots, 13\}$ are out of the eclipse. A large fraction of the exposure time was lost for $i_{\text{orb}} = 13$ due to ADR recycling. The quoted errors hereafter represent 1σ statistical uncertainty.

3. Analysis

3.1. Spectra

Figure 2(a) shows the broadband spectrum with Resolve integrated over the entire off-eclipse phase. Upon the hard continuum emission, emission lines of highly ionized S and Fe as well as the fluorescence of neutral or low-ionized Fe are

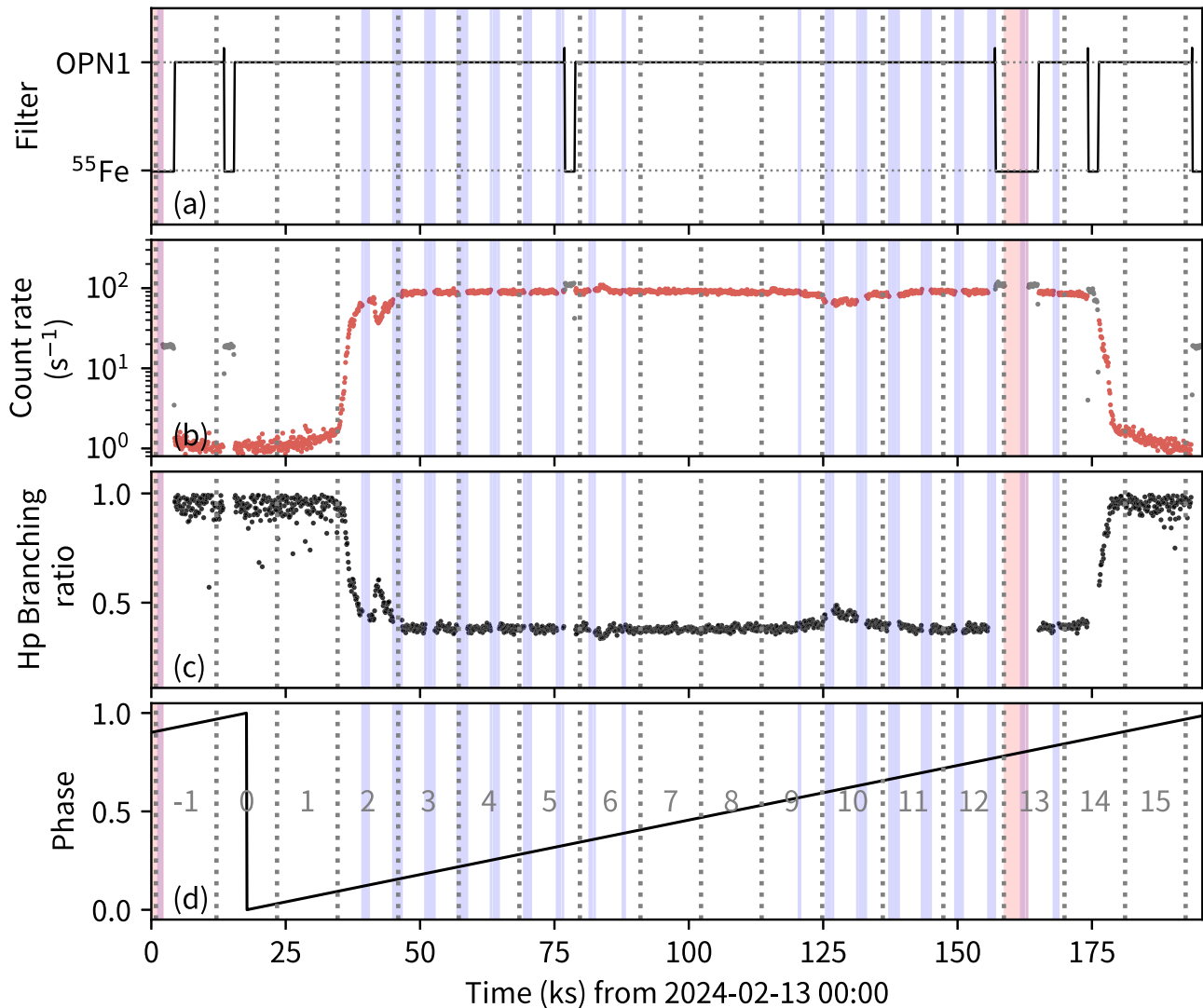


Figure 1. (a) FW positions, (b) 2–12 keV count rate binned at 100 s, (c) the fraction of Hp events, and (d) orbital phase (M. Falanga et al. 2015). The observation was interrupted by South Atlantic Anomaly passages (blue) and ADR recycles (red). The FW ^{55}Fe was illuminated several times as shown in (a) during on-source integration time, leading to an additional count rate of 20 s^{-1} .

evident. The Fe K band is particularly rich; Fe XXV He α and Fe XXVI Ly α lines are resolved. Their resonance lines exhibit a clear signature of the P Cygni profile.

Figure 2(b) shows the narrowband spectrum of the Fe K α line at two opposite orbital phases. The center energy is significantly displaced. We constructed the narrowband spectrum at each ϕ_{orb} bin and fitted the Fe K α line with an empirical model consisting of a handful of Lorentzian profiles (G. Hölzer et al. 1997). The free parameters are the center energy, width, and normalization for the set of the lines, and the index and normalization of the underlying power-law continuum. Fe K α lines broader than the one presented here may additionally exist, but it is not required in the narrowband fitting. The best-fit values are shown in Figures 3(a)–(c).

To validate the result, we also fitted the Mn K α and K β lines of the electron capture decay of ^{55}Fe during the FW ^{55}Fe illuminations in the same data set. The G. Hölzer et al. (1997) model with corrections based on the microcalorimeter data¹³ was used. The energy of the Mn K α (Mn K β) line is

accurate to 0.06 ± 0.01 (0.31 ± 0.04 eV) equivalent to 3.0 ± 0.6 (15 ± 2) km s^{-1} . The broadening besides the instrumental line spread function is $<5 \times 10^{-4}$ ($<10^{-4}$) eV equivalent to $<2 \times 10^{-2}$ ($<10^{-2}$) km s^{-1} .

The RV dependence on ϕ_{orb} (Figure 3(a)) shows a clear sinusoidal pattern. We fitted the data outside of the eclipse with a sine curve and obtained the best-fit RV amplitude of 248 ± 13 km s^{-1} , the RV offset of -140 ± 4 km s^{-1} , and the phase offset of 0.004 ± 0.001 . The phase offset is consistent with null. The RV offset is larger than the arithmetic sum of the gain uncertainty and XRISM motion around the solar barycenter ($+15$ km s^{-1}). We attribute the rest to the proper motion of Cen X-3 (-39 km s^{-1} ; J. B. Hutchings et al. 1979) and other factors.

The line flux (Figure 3(b)) also exhibits a change as a function of ϕ_{orb} with approximately a single peak profile outside of the eclipse. During the eclipse, the line flux is reduced but not null, which is consistent with the previous measurements (N. Aftab et al. 2019). The line width (Figure 3(c)) is significantly broader than null across ϕ_{orb} with 10–20 eV corresponding to 500–1000 km s^{-1} in FWHM. If the

¹³ https://heasarc.gsfc.nasa.gov/docs/hitomi/calib/hitomi_caldb_docs.html

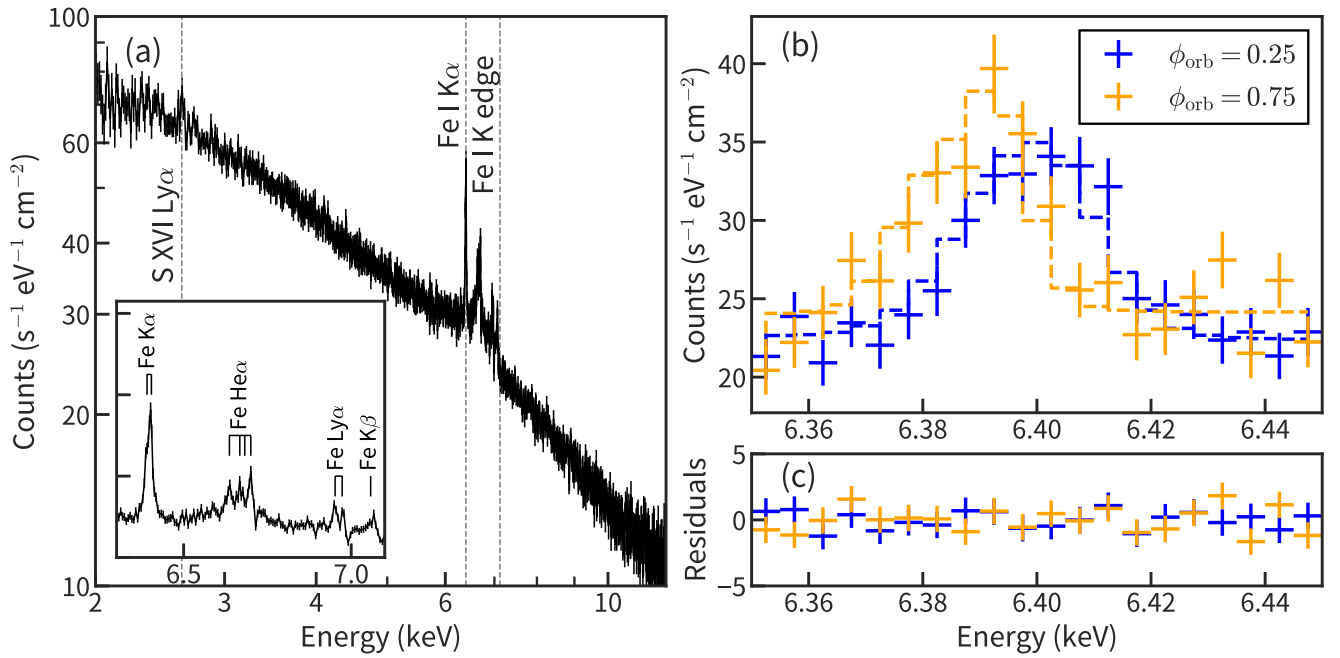


Figure 2. (a) Resolve spectra out of the eclipse in the 2–12 keV band. A close-up view of the Fe K band is given in the inset. (b) Fe $K\alpha$ spectra and their best-fit models and (c) residuals to the fit at $\phi_{\text{orb}} = 0.25$ (blue) and 0.75 (orange). Compare to Figure 4 (a) in P. S. Wojdowski et al. (2003) for previously the best spectra with the Chandra grating spectrometer.

broadening did not exist, the $K\alpha^1$ and $K\alpha^2$ lines would have been easily resolved (Figure 2(b)).

We evaluated the EW as well as the fluorescence equivalent width (fEW) of the Fe $K\alpha$ line (Figure 3(d)). Here, fEW is defined as the line intensity divided by the continuum flux at 7.10–7.11 keV just below the Fe K edge energy. The metric is more physical for the fluorescence line than the conventional EW that uses the continuum flux at the line energy, but fEW and EW are different only by a small factor (~ 1.1). The fEW can be assessed for the first time with Resolve without being contaminated by the associated Fe $K\beta$ line at 7.05 keV. The fEW shows a relatively flat distribution over ϕ_{orb} out of the eclipse and a much larger value during the eclipse.

3.2. Timing

For all events, we corrected for the arrival times due to the XRISM motion around the barycenter of the solar system and the NS motion around the center of mass (CoM) in the Cen X-3 system. We then derived the spin period $P_{\text{spin}} = 4.79784$ s using the epoch folding search. The pulse profile is made for different broad energy bands as well as a narrow band containing the Fe $K\alpha$ (6.35–6.45 keV) and is normalized to the average (Figure 4(a)). Here, the use of all event grades is important, as the grade branching ratio changes as a function of pulse phase.

The pulse profile is similar, but different, among the different energy bands. We derived the pulse delay relative to the lowest energy band by cross-correlating the profiles (Figure 4(b)). We also derived the pulse fraction as the peak-to-peak value of the normalized profile (Figure 4(c)). By comparing between the 7–8 keV (ionizing photons) and Fe $K\alpha$ band (fluorescent photons), we found no significant phase delay but a significant drop in pulse fraction in Fe $K\alpha$. The decrement of the pulse fraction at the Fe K band was reported in low-resolution timing spectroscopy (C. Ferrigno et al. 2023), which is now revealed to be associated to the Fe $K\alpha$ fluorescence line.

4. Discussion

In Cen X-3, the Roche lobe is considered to be filled, and the accretion disk is formed around the NS. The matter from the O star accretes through the first Lagrangian point (L1) via the accretion stream to the outer part of the accretion disk, which is truncated at an inner radius, where magnetic pressure dominates. See also Figure 10 in S. S. Tsygankov et al. (2022).

The system scale is shown in Figure 5. The radius of the O star is approximated by the effective Roche-lobe radius $R_O = 0.62a$ for the mass ratio $M_{\text{NS}}/M_O = 0.059$ (P. P. Eggleton 1983). This is consistent with the value ($0.62a$) derived from the eclipse duration (M. Mouchet et al. 1980). When viewed from the NS, the O star subtends $\Delta\Omega_O = 2\pi(1 - \cos\theta_0)$ str, where $\theta_0 = \arcsin(R_O/a)$. For $R_O = 0.62a$, $\Delta\Omega_O/4\pi = 0.1$. The light travel distance for the spin period is $P_{\text{spin}}c = 0.11a$. Below, we consider several possibilities for the production site of the Fe $K\alpha$ line.

First, it has been postulated that the most plausible location of the reprocessing cold matter is the vicinity of NS for two major reasons: (1) the line intensity drops during the eclipse (F. Nagase et al. 1992; K. Ebisawa et al. 1996; S. Naik et al. 2011) using the data taken with Ginga, ASCA, and XMM-Newton, and (2) the line photons are delayed in the pulse phase only by 0.39 ms (T. Kohmura et al. 2001) corresponding to $\sim 10^{-5}a$. If the reprocessing matter is so close to the NS, we would expect the RV of the line to be modulated by the NS motion with an amplitude of $2\pi a_{\text{NS}} \sin i / P_{\text{orb}} = 391 \pm 8 \text{ km s}^{-1}$, where $a_{\text{NS}} = aM_O/(M_{\text{NS}} + M_O)$ is the radius of the NS orbit around the CoM of the binary (red circle in Figure 5). The actual measurement is significantly smaller (Figure 3). Also, it does not explain the decrement of the pulse fraction at the Fe $K\alpha$ band (Figure 4(c)).

Second, we consider the surface of the O star as the site of reprocessing. This would naturally explain the RV amplitude if the O star surface rotates synchronously with the NS orbital motion. To take into account three-dimensional effects, we

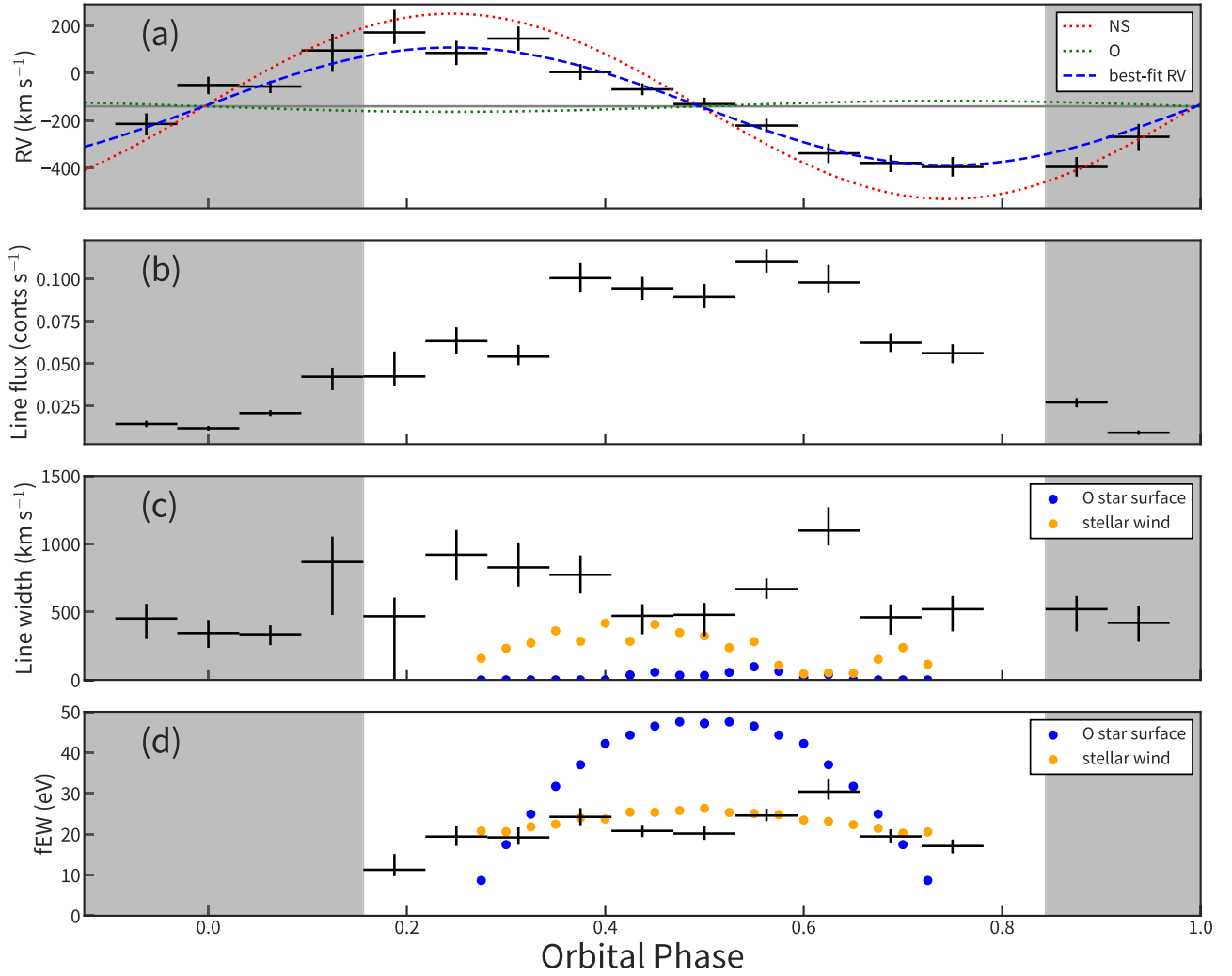


Figure 3. Best-fit values of (a) Fe K α line center, (b) flux, and (c) width as well as (d) fEW as a function of ϕ_{orb} . Shaded areas indicate eclipses. In (a), the data are compared to the RV curve of the NS (red), O star (green), and the best fit to the data outside the eclipse (blue). Positive RVs are in the approaching direction. Results of the radiative transfer calculation are compared in (c) and (d) for the O star surface (blue) and stellar wind (orange) as the site of Fe K α production.

performed a radiative transfer calculation using SKIRT (B. Vander Meulen et al. 2023), which is a three-dimensional Monte Carlo solver. The setup is shown in Figure 5. We assumed that the O star fills the Roche lobe and the reflection takes place on its skin surface with a density of 10^{18} cm^{-3} but with no velocity. We launched photons isotropically from the point-like NS placed at varying ϕ_{orb} . The incident photons are sampled to follow a power-law spectral shape with a photon index of 1.5 in the 2–50 keV range. We considered the X-ray photon interactions with matter in the O star for photoionization, fluorescence, and electron scattering. We derived the fEW as a function of ϕ_{orb} and compared it with the data (Figure 3(d)). A large discrepancy is found both in the absolute value and the ϕ_{orb} dependence. The contribution by the O star surface reflection is unavoidable for its large subtended angle and should be dominant as long as the radiation from the NS is isotropic. The result infers that the emission from the NS is highly nonisotropic and most of its emission is not subtended by the O star surface. The same result was found in another eclipsing HMXB Vela X-1 by R. Rahin & E. Behar (2023), who argued against the reprocessing on the companion star surface.

Third, we consider cold matter in the line of sight. Its column density can be derived from the Fe K edge depth (τ_{Fe}) at the edge energy $E_e = 7.12 \text{ keV}$. The fEW should be proportional to τ_{Fe} for an optically thin case. We used SKIRT in a different configuration, in which a point-like NS placed at the center is surrounded by a shell with a thickness corresponding to τ_{Fe} . Clumping of matter in the shell is also considered with a parameter f , which is the fraction of total mass in clumps. The remaining $1 - f$ of mass is distributed uniformly in the shell. Figure 6 shows the observed and simulated results. The absolute value of fEW as a function of τ_{Fe} was not well reproduced with $f=0$ (uniform density without clumps) but was with $f=0.15$. This idea also explains some previous observations (S. Naik et al. 2011; G. Sanjurjo-Ferrín et al. 2021), in which Fe K α was found to be much more intense with $\text{EW} > 100 \text{ eV}$. The variation of its intensity is correlated well with the line-of-sight partial-covering column density derived from the broadband spectral fitting. Note that the XRISM observation was made when the line-of-sight column is smaller than these observations.

What is, then, the cold matter that produces the Fe K α line in the line of sight? The present results require the following conditions. First, it has an RV amplitude smaller than that of

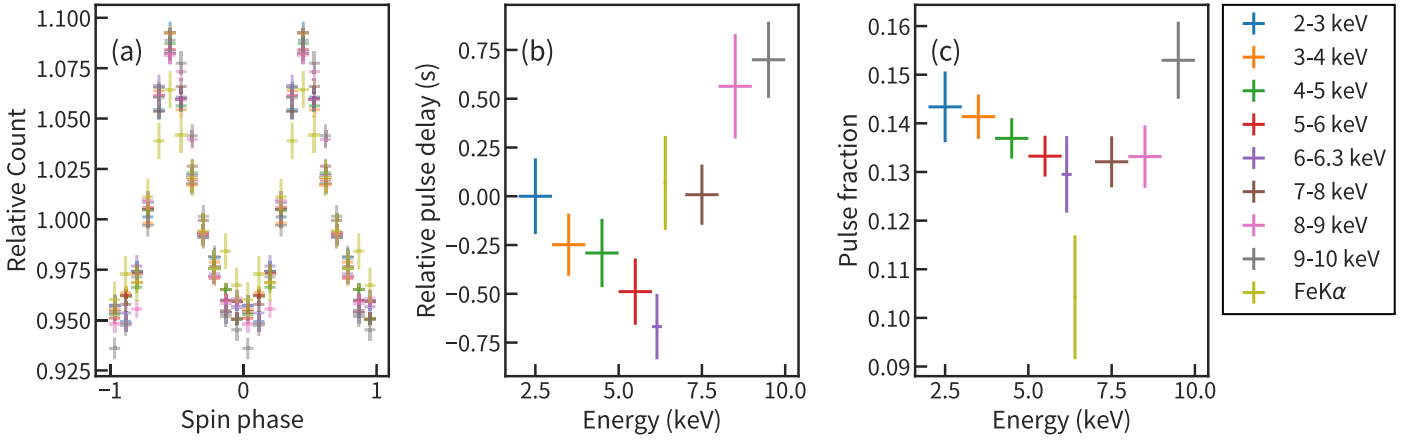


Figure 4. (a) Pulse shape folded by P_{spin} , (b) phase delay relative to the lowest energy band as a function of energy, and (c) pulse fraction as a function of energy. The Fe K α count rate is from 6.35 to 6.45 keV.

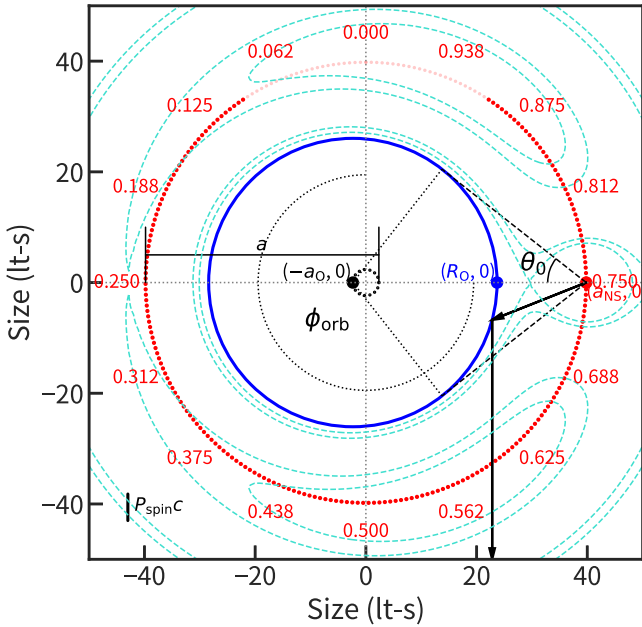


Figure 5. Schematic view and the radiative transfer calculation setup at $\phi_{\text{orb}} = 0.75$. The CoM is placed at the origin, and the orbit is projected on its plane. The line of sight is toward +y-axis direction. The locations of the NS (red), O star (black), and an O star surface closest to the NS (blue) are shown with filled circles of their colors. The NS and O star orbits are shown with dotted circles. For the NS orbit, the eclipsed part is shown in transparency, and ϕ_{orb} is shown in text. The Roche potential is shown with the turquoise contours. The scale length of $P_{\text{spin}} c$ is shown at the bottom left. For the modeling, the O star surface is approximated by a sphere with a radius of R_O in blue, which subtends an angle θ_0 seen from the NS. A reflection path is shown with black arrows.

the NS (Figure 3(a)). Second, it has a velocity dispersion of $500\text{--}1000 \text{ km s}^{-1}$ in FWHM (Figure 3(c)). Third, its density (n) should be high enough so that the matter remains neutral or low ionized under a radiation field of $L_X \sim 10^{37} \text{ erg s}^{-1}$, i.e., the ionization parameter ($\xi = \frac{L_X}{nr^2}$; C. B. Tarter et al. 1969) should be less than ~ 10 (T. R. Kallman et al. 2004). This requires $n \gtrsim 10^{12} (r/a)^{-2} \text{ cm}^{-3}$, where r is the distance from the NS to the cold matter. This further constrains the physical thickness of matter (d) to be $d < 0.04a(r/a)^2 \text{ cm}$ from $\tau_{\text{Fe}} = dnA_{\text{Fe}}\sigma_K$, where A_{Fe} is the abundance of Fe relative to H (E. Anders &

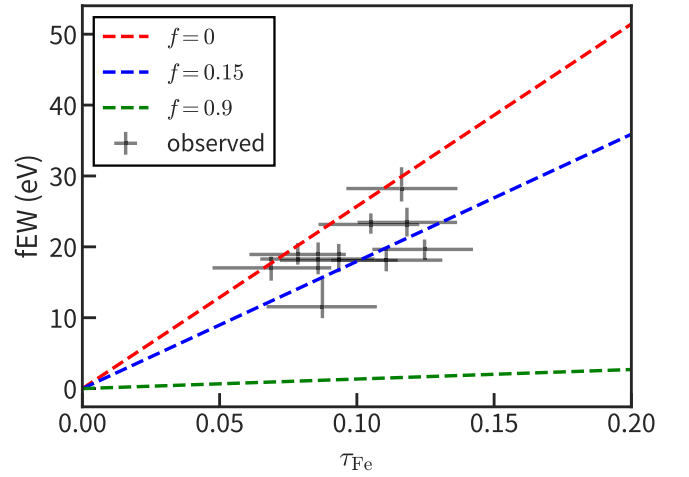


Figure 6. Relation between τ_{Fe} and $f\text{EW}$. The observed results at different ϕ_{orb} are shown with plus symbols, while the simulated results are shown with dotted lines of different colors for different $f \in \{0, 0.15, 0.9\}$.

N. Grevesse 1989), and σ_K is the photoelectric absorption cross section at the edge of Fe K.¹⁴ Fifth, d needs to have some scatter of $\approx P_{\text{spin}} c$, so that the coherent pulse signal of the NS will spread over the spin phase so that the reprocessed emission is consistent with the lack of phase delay and the reduced pulse fraction (Figure 4).

We list two possibilities. One is the stellar wind as argued for QV Nor (J. M. Torrejón et al. 2015). We ran another SKIRT simulation for a stellar wind having a spherically symmetric density and velocity distributions. We assumed a constant wind mass-loss rate $0.2 \times 10^{-6} M_{\odot} \text{ yr}^{-1}$, the RV following the $\beta = 1.0$ law with the terminal velocity 1000 km s^{-1} , and the azimuthal velocity with the same angular velocity with NS. This yielded a good match for $f\text{EW}$ dependence on ϕ_{orb} (Figure 3(d)), as the stellar wind is distributed more largely than the O star surface. Yet, it fails to explain the observed velocity dispersion (Figure 3(c)).

The other is the accreting matter from L1 to the NS illuminated by the nonisotropic incident emission from the NS. An accretion stream trailing behind the NS is formed (A. Manousakis & R. Walter 2015; I. El Mellah et al. 2018), which is a candidate for such a matter. This is in agreement

¹⁴ We used the NIST Standard Reference Database 8.

with the recent measurement of the polarization of the X-ray continuum emission, which is an independent and complementary method to assess the reprocessing of the incident emission from the NS. Using IXPE (M. C. Weisskopf et al. 2022), S. S. Tsygankov et al. (2022) revealed polarized X-rays with the degree of polarization modulated by the NS spin phase. They argued that the polarization is made intrinsically as well as by reprocessing by the accreting matter to the NS.

5. Conclusion

We presented the result of X-ray microcalorimeter observations with the Resolve instrument on board XRISM using the data obtained during the performance verification phase. Cen X-3 was observed for its entire orbital phase using a 155 ks exposure at a high observing efficiency of 79%. We focused on the Fe $K\alpha$ emission line and revealed its new spectroscopic features as a function of the orbital phase and new timing features as a function of the spin phase using the unique capability of the Resolve instrument.

We examined several possibilities for the production site of the Fe $K\alpha$ emission, including the NS surface, O star surface, O star wind, and accretion stream through L1. We ran radiative transfer calculation for some of them, assuming spherically symmetric distributions of the density and velocity as well as the isotropic distribution of the X-ray illumination from NS. These assumptions are likely too simplistic to explain the rich observed phenomenology, which point toward the need for better modeling of such distributions. In other words, we can constrain them through the present observational results.

We demonstrated, in a practical use case, that the X-ray microcalorimeter can reveal new aspects of the Fe $K\alpha$ line, which is a powerful probe in many objects. As shown, we only used a small fraction of the 9 million events. Other aspects of the data and implications for their results will follow.



Acknowledgments








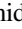


The authors thank all those who contributed to the XRISM mission. Richard Mushotzky provided useful comments on the manuscript. The anonymous reviewer pointed out that the stellar wind can be a production site of the Fe $K\alpha$ emission. This work was supported by the JSPS Core-to-Core Program (grant No. JPJSCCA20220002) and by NASA under the award number 80GSFC21M0002. This research made use of the JAXA's high-performance computing system JSS3. Y.M. is financially supported by the JST SPRING program (grant No. JPMJSP2108), B.V. by the Fund for Scientific Research Flanders (FWO-Vlaanderen, project 11H2121N). Part of this work was performed under the auspices of the U.S. Department of Energy by Lawrence Livermore National Laboratory under Contract DE-AC52-07NA27344. The material is based upon work supported by NASA under award number 80GSFC21M0002. C.D. acknowledges support from STFC through grant ST/T000244/1.

Facility: XRISM

Software: Xspec (v12.14.0h; K. A. Arnaud 1996), SKIRT (v9; B. Vander Meulen et al. 2023).

ORCID iDs

Yuto Mochizuki  <https://orcid.org/0000-0003-3224-1821>
Masahiro Tsujimoto  <https://orcid.org/0000-0002-9184-5556>

Richard L. Kelley  <https://orcid.org/0009-0007-2283-3336>
Bert Vander Meulen  <https://orcid.org/0000-0002-5488-1961>
Teruaki Enoto  <https://orcid.org/0000-0003-1244-3100>
Yutaro Nagai  <https://orcid.org/0009-0003-9261-2740>
Chris Done  <https://orcid.org/0000-0002-1065-7239>
Pragati Pradhan  <https://orcid.org/0000-0002-1131-3059>
Natalie Hell  <https://orcid.org/0000-0003-3057-1536>
Katja Pottschmidt  <https://orcid.org/0000-0002-4656-6881>
Ken Ebisawa  <https://orcid.org/0000-0002-5352-7178>
Ehud Behar  <https://orcid.org/0000-0001-9735-4873>

References

- Aftab, N., Paul, B., & Kretschmar, P. 2019, *ApJS*, 243, 29
Anders, E., & Grevesse, N. 1989, *GeCoA*, 53, 197
Arnason, R. M., Papei, H., Barnby, P., Bahramian, A., & D. Gorski, M. 2021, *MNRAS*, 502, 5455
Arnaud, K. A. 1996, in ASP Conf. Ser. 101, *Astronomical Data Analysis Software and Systems V*, ed. G. Jacoby & J. Barnes (San Francisco, CA: ASP), 17
Ash, T. D., Reynolds, A. P., Roche, P., et al. 1999, *MNRAS*, 307, 357
Bildsten, L., Chakrabarty, D., Chiu, J., et al. 1997, *ApJS*, 113, 367
Canizares, C. R., Davis, J. E., Dewey, D., et al. 2005, *PASP*, 117, 1144
Chodil, G., Mark, H., Rodrigues, R., et al. 1967, *PhRvL*, 19, 681
de Vries, C. P., Haas, D., Yamasaki, N. Y., et al. 2017, *JATIS*, 4, 1
Ebisawa, K., Day, C. S., Kallman, T. R., et al. 1996, *PASJ*, 48, 425
Eggleton, P. P. 1983, *ApJ*, 268, 368
El Mellah, I., Sundqvist, J. O., & Keppens, R. 2018, *MNRAS*, 475, 3240
Ezoe, Y., Ishisaki, Y., Fujimoto, R., et al. 2020, *Cryo*, 108, 103016
Falanga, M., Bozzo, E., Lutovinov, A., et al. 2015, *A&A*, 577, A130
Ferrigno, C., D'Al, A., & Ambrosi, E. 2023, *A&A*, 677, A103
Giacconi, R., Gursky, H., Kellogg, E., Schreier, E., & Tananbaum, H. 1971, *ApJL*, 167, L67
Hölzer, G., Fritsch, M., Deutsch, M., Härtwig, J., & Förster, E. 1997, *PhRvA*, 56, 4554
Hutchings, J. B., Cowley, A. P., Crampton, D., van, J., & White, N. E. 1979, *ApJ*, 229, 1079
Ishisaki, Y., Yamada, S., Seta, H., et al. 2018, *JATIS*, 4, 011217
Ishisaki, Y., Kelley, R. L., & Awaki, H. 2022, *Proc. SPIE*, 12181, 121811S
Kallman, T. R., Palmeri, P., Bautista, M. A., Mendoza, C., & Krolik, J. H. 2004, *ApJS*, 155, 675
Kelley, R. L., Rappaport, S., Clark, G. W., & Petro, L. D. 1983, *ApJ*, 268, 790
Kilbourne, C. A., Adams, J. S., Brekosky, R. P., et al. 2016, *Proc. SPIE*, 9905, 99053L
Kilbourne, C. A., Sawada, M., Tsujimoto, M., et al. 2018, *PASJ*, 70, 18
Klawin, M., Doroshenko, V., Santangelo, A., et al. 2023, *A&A*, 675, A135
Kohmura, T., Kitamoto, S., & Torii, K. 2001, *ApJ*, 562, 943
Krzeminski, W. 1974, *ApJL*, 192, L135
Manousakis, A., & Walter, R. 2015, *A&A*, 575, A58
Midooka, T., Tsujimoto, M., Kitamoto, S., et al. 2021, *JATIS*, 7, 028005
Mizumoto, M., Tsujimoto, M., Cumbee, R., et al. 2022, *Proc. SPIE*, 12181, 121815Z
Mochizuki, Y., Tsujimoto, M., Kilbourne, C. A., et al. 2024, *Proc. SPIE*, 13093, 1309363
Mouchet, M., Illovaisky, S. A., & Chevalier, C. 1980, *A&A*, 90, 113
Nagase, F., Corbet, R. H. D., Day, C. S. R., et al. 1992, *ApJ*, 396, 147
Naik, S., Paul, B., & Ali, Z. 2011, *ApJ*, 737, 79
Omama, T., Tsujimoto, M., Sawada, M., et al. 2022, *Proc. SPIE*, 12181, 1218162
Porter, F. S., Chiao, M. P., Eckart, M. E., et al. 2016, *JLTP*, 184, 498
Rahin, R., & Behar, E. 2023, *ApJ*, 950, 170
Sanjurjo-Ferrin, G., Torrejón, J. M., Postnov, K., et al. 2021, *MNRAS*, 501, 5892
Sato, K., Uchida, Y., & Ishikawa, K. 2023, in *High-Resolution X-ray Spectroscopy: Instrumentation, Data Analysis, and Science*, ed. C. Bambi & J. Jiang (Singapore: Springer), 93
Schreier, E., Levinson, R., Gursky, H., et al. 1972, *ApJL*, 172, L79
Seta, H., Tashiro, M. S., Ishisaki, Y., et al. 2012, *IEEE*, 59, 366
Shirron, P. J., Kimball, M. O., James, B. L., et al. 2016, *Proc. SPIE*, 9905, 990530
Suchy, S., Pottschmidt, K., Wilms, J., et al. 2008, *ApJ*, 675, 1487
Tamba, T., Odaka, H., Tanimoto, A., et al. 2023, *ApJ*, 944, 9
Tarter, C. B., Tucker, W. H., & Salpeter, E. E. 1969, *ApJ*, 156, 943

- Tashiro, M. S., Maejima, H., & Toda, K. 2020, [Proc. SPIE, 11444, 1144422](#)
- Torrejón, J. M., Schulz, N. S., Nowak, M. A., & Kallman, T. R. 2010, [ApJ, 715, 947](#)
- Torrejón, J. M., Schulz, N. S., Nowak, M. A., et al. 2015, [ApJ, 810, 102](#)
- Tsygankov, S. S., Doroshenko, V., Poutanen, J., et al. 2022, [ApJL, 941, L14](#)
- Tzanavaris, P., & Yaqoob, T. 2018, [ApJ, 855, 25](#)
- van der Meer, A., Kaper, L., van Kerkwijk, M. H., Heemskerk, M. H., & van den Heuvel, E. P. 2007, [A&A, 473, 523](#)
- Vander Meulen, B., Camps, P., Stalevski, M., & Baes, M. 2023, [A&A, 674, A123](#)
- Weisskopf, M. C., Soffitta, P., Baldini, L., et al. 2022, [JATIS, 8, 026002](#)
- Wojdowski, P. S., Liedahl, D. A., Sako, M., Kahn, S. M., & Paerels, F. 2003, [ApJ, 582, 959](#)